IEEE Access
Multidisciplinary ⋮ Rapid Review ⋮ Open Access Journal

Received 13 August 2023, accepted 31 August 2023, date of publication 5 September 2023, date of current version 12 September 2023.

Digital Object Identifier 10.1109/ACCESS.2023.3312122

RESEARCH ARTICLE

A Compact Two-Element Linearly and Orthogonal Circularly Polarized MIMO Antenna System for 5G Cellular and WLAN/Wi-Fi 6E Application

WATHEQ A. NEAMAH[1,2], HAIDER M. AL SABBAGH[1], (Senior Member, IEEE), AND HUSSAIN AL-RIZZO[3]

[1]Department of Electrical Engineering, College of Engineering, University of Basrah, Basrah 61004, Iraq
[2]College of Engineering, University of Thi-Qar, Nasiriyah 64001, Iraq
[3]Department of Systems Engineering, University of Arkansas at Little Rock, Little Rock, AR 72204, USA

Corresponding author: Watheq A. Neamah (watheq.neamah@utq.edu.iq)

ABSTRACT This paper presents the design, analysis, and experimental validation of a compact 2×1 MIMO antenna operating in two bands. Band 1 is Linearly Polarized (LP) with spatial diversity operating in the sub-6 GHz band for the Fifth Generation (5G). Band 2 is Circularly Polarized (CP) for polarization and pattern diversity with an axial ratio below 3 dB for WLAN, Wi-Fi 6E, and C-band applications. The proposed single antenna consists of a Squared Shape Modified Monopole with partially Defected Ground (SMMDG) fed by Co-Planar Waveguide CPW. The partial ground has a defect on its upper left side and an I-shaped strip on the right side. The two MIMO radiators are arranged in oppositely flipped shapes. The decoupling and common partial ground structure consists of an opposite, Double T-shaped strip (DTSS) with a common strip head that performs as a band-stop filter. The overall dimensions of the MIMO antenna are $31.5 \times 45 \times 1.6$ mm^3. The simulated impedance bandwidth of the first band with LP lies between 3.1 and 4.7 GHz, for which S_{11} and $S_{22} < -10$ dB, while the measured values are between 3.45 GHz and 4.8 GHz. The simulated impedance bandwidth for the second band for S_{11} and $S_{22} < -10$ dB lies between 5.24 and 7.9 GHz, while the measured one lies between 5.65 GHz and 9 GHz. The simulated 3-dB Axial Ratio Bandwidth (ARBW) within Band 2 is (5.6–8.5) GHz, while the measured 3-dB ARBW is (5.95–8.1) GHz. The minimum simulated isolation between the two ports is 17 dB in Band 1 and 26 dB in Band 2, while the minimum measured isolation is 21 dB in Band 1 and 26 dB in Band 2. Wi-Fi 6E (n96) (5.925-7.125) GHz is covered with right-hand circular polarization (RHCP) in the positive Z direction and left-hand circular polarization (LHCP) in the negative Z direction, covering Band 2 with an axial ratio less than 3 dB. Other crucial MIMO metrics are also calculated, such as the Envelope Correlation Coefficient (ECC), Mean Effective Gain (MEG), and Diversity Gain (DG). The antenna provides excellent MIMO diversity performance, which makes it an excellent candidate for many portable wireless applications.

INDEX TERMS Dual band, low profile, sub 6 band, Wi-Fi 6E, circularly polarized, MIMO antenna.

I. INTRODUCTION

5G-enabled MIMO wireless systems enable greater range, higher data rates, lower latencies, improved mobility, and more reliable connections through spatial multiplexing and diversity techniques [1]. The world is transitioning to 5G technology to accommodate the exponential rise of global mobile data traffic and the billions of existing wireless devices [2]. Due to its capacity to transmit large amounts of data across vast distances, the sub-6 GHz band is an excellent choice for 5G systems [3], [4]. A multi-band antenna is always better than separate antennas operating at different frequencies. The size of the antennas is a limiting factor for many communication devices, including those with MIMO systems.

However, the existing wireless network technology limits download speeds for applications such as 4K and 8K video and the Internet of Things (IoT). Current WLAN upload and

The associate editor coordinating the review of this manuscript and approving it for publication was Jiankang Zhang.

This work is licensed under a Creative Commons Attribution-NonCommercial-NoDerivatives 4.0 License.
For more information, see https://creativecommons.org/licenses/by-nc-nd/4.0/

download rates are considered poor for these recent applications. Wi-Fi 6E, a new generation proposed by Wi-Fi Alliance in 2021, has a bandwidth between 5.925 and 7.125 GHz, with 14 80 MHz or 7 channels of 160 MHz [5]. MIMO antennas play a crucial role in 5G communication systems because they can improve connection reliability and channel capacity without increasing the power or bandwidth [6]. Voluminous studies have been reported on the design of MIMO antennas with polarization and spatial diversity, including cellular and indoor wireless systems, radar, vehicular, wearable antennas, imaging, Wireless Body Area Networks (WBAN), wireless local area networks (WLAN), tumor detection, and 5G communication technologies [7], [8], [9], [10].

Regarding signal propagation, CP antennas provide significant benefits over LP antennas [11]. A comparative examination of the MIMO performance achieved with orthogonal CP radiators against orthogonal LP radiators was investigated in [12]. It is concluded that CP radiators achieved eigenvalues higher than LP radiators. When LP MIMO antennas are not properly aligned, the channel capacity of the CP antennas exceeds that of the LP radiators [13], [14].

Various microstrip antennas with LP and CP have been reported due to their favorable features of being easy to build on multi-element-circuitry, low profile, and low weight [15]. Polarization misalignment between the transmitting and receiving antennas leads to polarization mismatch losses for the LP antenna. CP antennas benefit many communication systems since antenna orientation is unnecessary, and the received signal intensity is relatively consistent despite antenna direction [16]. Due to these benefits, CP antennas are desirable for various wireless applications, including GPS.

Recent research has concentrated on decoupling techniques, particularly for wideband MIMO antennas. Although these decoupling structures have improved the isolation between MIMO elements, most of these solutions are complicated or introduce extra space for the design [17]. It can be achieved using C-shaped parasitic decoupling structures [18]. Employing neutralized line (NL) techniques constructs an antiphase current route to the coupling between array elements [19]. In addition, antenna decoupling surfaces (ADS) may eliminate coupling by reflecting it into space. It is done by loading a thin substrate with a grid of small metal elements [20]. Defected Ground Structure (DGS) is another technique used to reduce ground current on antenna arrays; it involves slicing slots into the antenna by periodic or non-periodic patterns [21], [22].

In this paper, a versatile MIMO antenna design is introduced, analyzed, and experimentally validated for a two-port MIMO antenna, dual-band, operating in the sub-6 GHz for 5G, WLAN, and Wi-Fi 6E applications. The single element comprises a modified SMMDG shape fed by CPW. The partial ground is changed at its top left side, making it shorter than the right side, which added an I-shape strip to its side. The frequency response for band 1 (sub-6 GHz) covers the n77 and n78 sub-bands with LP over 3.5-4.5 GHz bandwidth, over which S_{11} and $S_{22} < -10$ dB. The second band lies between 5.6 GHz and 8 GHz, where S_{11} and $S_{22} < -10$ with a CP of 3-dB ARBW over the frequency range from 5.9 GHz to 8.5 GHz. The isolation structure between the antenna parts is a simple DTSS that also serves as a common ground band stop filter.

The paper is organized as follows. Section II introduces the design procedure and the parametric study of the single antenna element. Section III discusses the proposed MIMO antenna configuration and presents simulated and experimental results of the scattering parameters and radiation patterns. The MIMO performance metrics are introduced in Section IV. Section V compares the prototype's findings against the recent state-of-the-art. Finally, conclusions are summarized in Section VI.

II. SINGLE-ELEMENT DESIGN PROCEDURE

Figure 1 depicts the geometry for the proposed single-element SMMDG. The SMMDG antenna is printed on only one side of an FR-4 substrate with a 4.4 dielectric constant; the loss tangent is 0.02. A 50 Ω CPW feeds. The antenna's metal coat is 0.035 mm copper cladding, widely available in FR4 substrates.

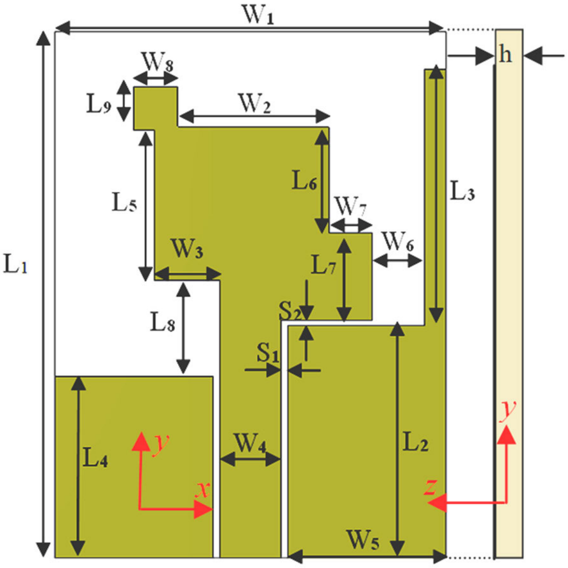

FIGURE 1. The geometry of the proposed SMMDG single-element antenna.

All the simulations are conducted using CST Microwave Studio software. Table 1 summarizes the dimensions of each parameter used in the design. Figure 2 shows the four steps of development that led to the find proposed design. The first three phases concentrate on getting resonance in the targeted bands. The square element radiator dimensions are calculated using [23] and shown in Fig. 2(a). For compact operation, we apply DGS on the partial ground to produce parasitic capacitance by widening fringing fields, enhancing the coupling between the element and ground, and improving

TABLE 1. **Design parameters and dimensions for the proposed (SMMDG) antenna.**

Parameter	Value (mm)	Parameter	Value (mm)	Parameter	Value (mm)
W_1	18	W_6	2.4	L_3	11.7
W_2	6.95	W_7	2	L_4	8.3
W_3	3	W_8	2	L_5	6.85
W_4	2.8	L_1	25	L_6	4.8
W_5	7.3	L_2	10.6	L_7	4
L_8	4.35	L_9	2	h	1.6
S_1	0.3	S_2	0.3		

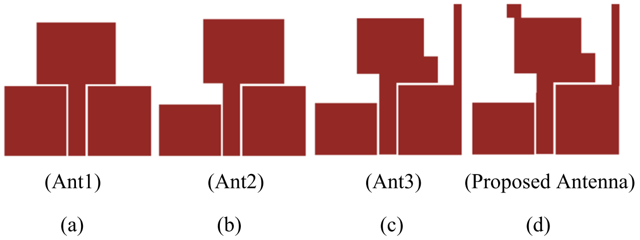

(a) (b) (c) (d)

FIGURE 2. **The geometrical progression of the SMMDG antenna.**

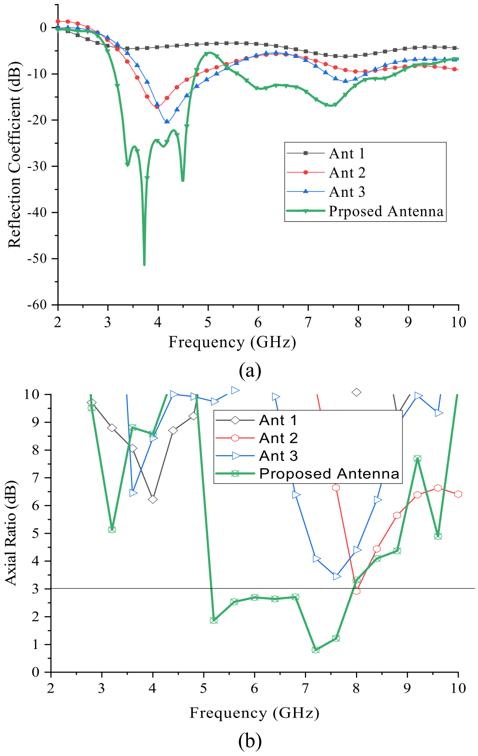

(a)

(b)

FIGURE 3. **Reflection coefficient and axial ratio SMMDG antenna.**

bandwidth. As shown in Fig. 2(b), besides introducing DGS to achieve the dual-band, the radiator element is shifted to the right side to excite more modes at the element.

The dual-band frequency responses are centered at 4 and 11 GHz, obtained by the configuration shown in Fig. 2 (b). Since the response at 11 GHz needs more shifts toward the range of 6 GHz to 7 GHz of the Wi-Fi 6E band, the element is truncated from the lower corner on the left side and at a rectangular cut is introduced at the top right of the element; this is shown in Fig. 2(c). As shown in Fig. 2(d), we introduced the I-shape strip and square-shaped stub to adjust the S_{11} spectrum to suit the intended bands and improve the axial ratio. Figure 3 shows the reflection coefficient and axial ratio related to the evolution of the geometric progression of the SMMDG.

A. PARAMETRIC STUDY

The I-shape strip is tuned to improve the frequency response and axial ratio. Fig. 4 depicts S_{11} and axial ratio versus frequency for various values of the I-shaped strip, which L3 denotes. As shown in Fig. 4(a), L_3 is changed from 2.7 mm to 11.7 mm. At 2.7 mm, S_{11} is not significantly enhanced for both bands. As L_3 is increased to 5.7 mm, S_{11} is enhanced for both bands; however, shifting to the Wi-Fi band is still needed. Although the -10 dB bandwidth of S_{11} with $L_3 = 8.7$ is enhanced for both bands, $L_3 = 11.7$ provides better results.

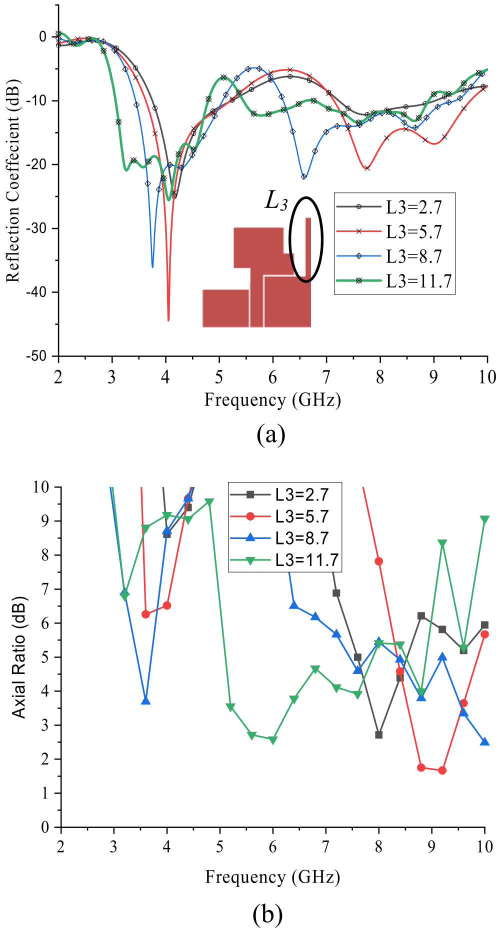

(a)

(b)

FIGURE 4. **Evolution of the L_3 effect on the reflection coefficient and axial ratio of the proposed SMMDG antenna.**

The first band, for which $S_{11}<-10$ dB, is confined between 3.1 GHz - 4.7 GHz, while the second band improved and is extended from 5.45 GHz to 8.6 GHz. In Fig. 4(b), the axial ratio versus frequency is depicted for the same values of the L_3 parameter range.

The axial ratios for all values of L_3 are not satisfied within the second band. The I-shaped strip significantly enhances the impedance bandwidth; however, the axial ratio is not satisfied within the desired range and is confined between 5.5 and 6 GHz. Hence, we propose a square-shaped stub structure to improve the axial ratio. The square-shaped stub is placed on the top of the radiator element. This square stub is sliding along the edge of the radiator element, starting from the right side at its middle and moving towards the left side of the radiator. Figure 5 shows the reflection coefficient and axial ratio versus frequency. The position of the square stub is denoted as (SL), which varies from 0 to 8 mm.

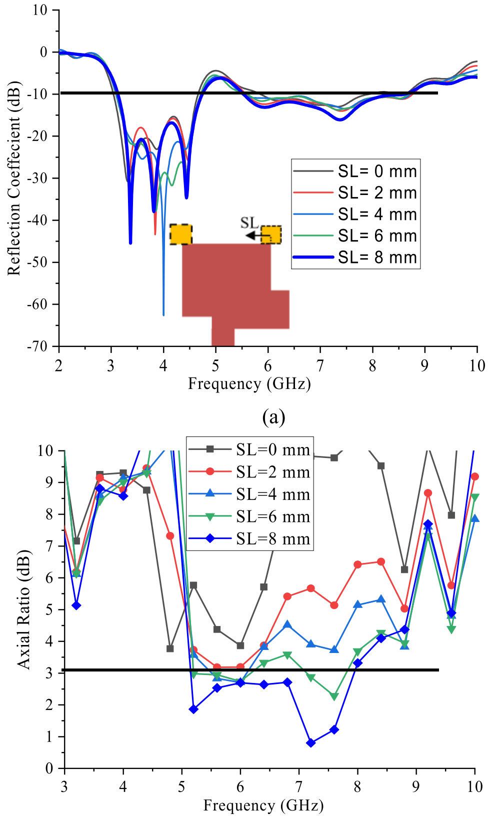

(a)

(b)

FIGURE 5. The effect of the SL parameter of the proposed SMMDG antenna.

As shown in Fig. 5(a), the reflection coefficients for all SL values are unaffected. Figure 5(b) shows that the axial ratio versus frequency is affected by stub sliding. The axial ratio reaches its targeted value of less than 3 dB at SL = 8 mm, which covers the band from 5.2 GHz to 8 GHz. At SL = 8 mm, the bandwidths of Band 1 and Band 2 of $S_{11} < -10$ dB are 3.15 GHz to 4.75 GHz and 5.5 GHz to 8.5 GHz, respectively.

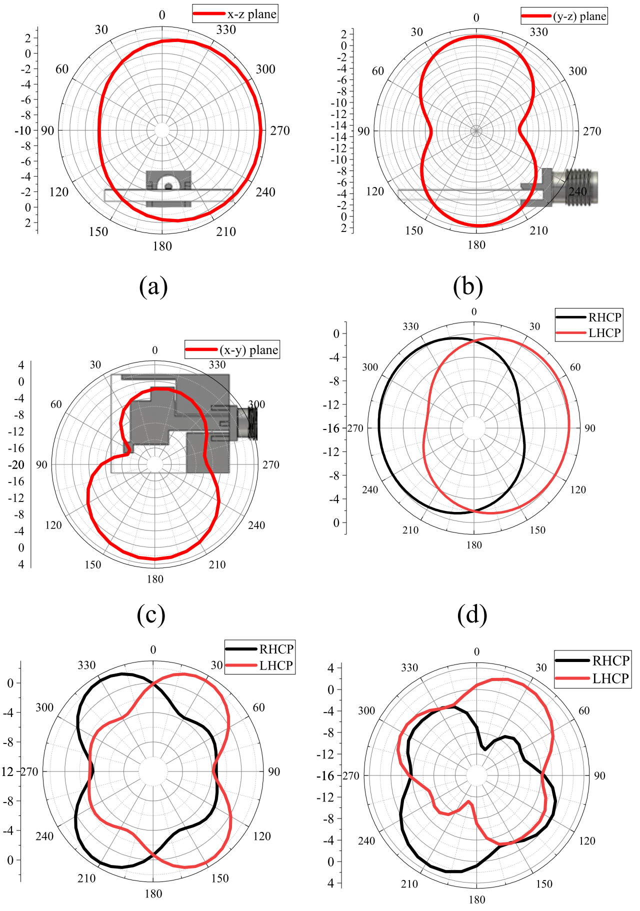

(a) (b)

(c) (d)

(e) (f)

FIGURE 6. The simulated radiation pattern of the SMMDG (a) (x-z) plane (Ø = 0°) at frequency 3.5 GHz (b) (y-z) plane (Ø = 90°) at frequency 3.5 GHz (c) (x-y) plane (Ø = 90°) at frequency 3.5 GHz (d) (x-z) plane (Ø = 0°) at frequency 6 GHz (e) (y-z) plane (Ø = 90°) at frequency 6 GHz. (f) (x-y) plane (Ø = 90°) at frequency 6 GHz.

B. RADIATION PATTERN

Figure 6 depicts the simulated radiation patterns versus the θ with $\emptyset = 0°$ for the (x-z) plane and $\emptyset = 90°$ for the (y-z) plane at frequencies of 3.5 GHz and 6 GHz. Figure 6(a) shows the pattern in the (x-z) plane at 3.5 GHz with a directive of 270 degrees. Figure 6 (b) shows the (y-z) plane pattern at 3.5 GHz that seems bean-shaped. Moreover, in Fig. 6(c), the pattern shown in the (x-y) plane, with $\theta = 90°$ versus the $\emptyset$, is at 3.5 GHz, showing a maximum point at 180 degrees. In Fig. 6(d), an RHCP of the (x-z) plane is shown at 6 GHz. Figure 6(e) shows an RHCP of the (y-z)-plane at 6 GHz. Figure 6(f) shows the pattern versus $\emptyset$ for $\theta = 90°$, corresponding to the (x-y) plane. The LHCP is a mirror image of the RHCP.

C. SURFACE CURRENT

Figure 7 depicts the surface current distribution of the antenna at four distinct phases (0°, 90°, 180°, and 270°) at 6.5 GHz.

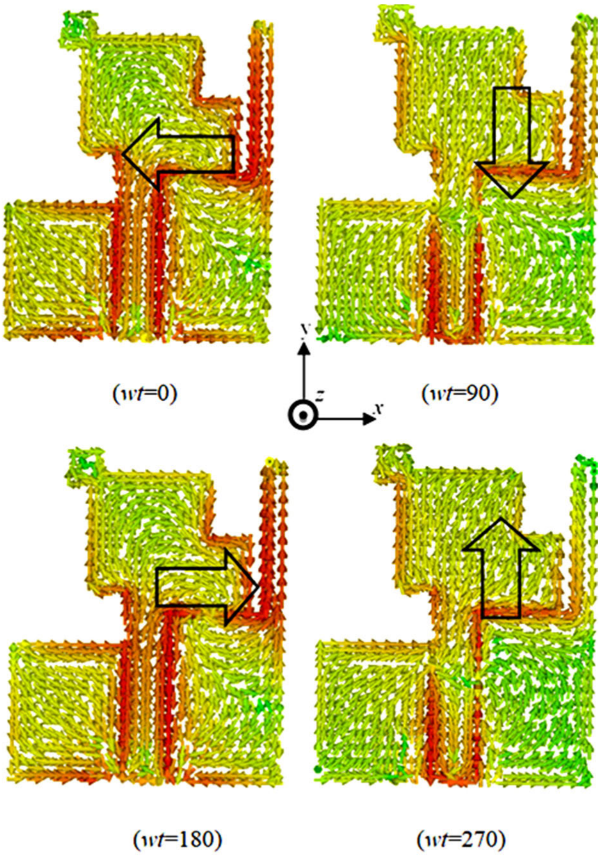

FIGURE 7. Simulated surface current distributions at 6. 5 GHz of the proposed antenna at four phases of excitations depicting RHCP in +Z direction.

Rotating surface current arrows are shown across the four phases to demonstrate the CP of the proposed antenna design. As the phase increases, it rotates in an anticlockwise sense in the +Z direction; hence, the antenna radiates RHCP waves at 6.5 GHz and LHCP in the -Z direction.

III. MIMO ANTENNA CONFIGURATION

In this section, we report the oppositely oriented two-element MIMO antenna. Fig. 8 illustrates the 2 × 1 MIMO configuration. The configuration illustrates the effect of element orientation on matching and isolation between the antenna ports. The minimum separation between the closest radiators is 0.2λ, where λ is the free-space wavelength at 3.5 GHz. To address the antenna's orientation, the I-shaped strip side of the antenna is called the "I-side," while the other side of the monopole is the front side. Fig. 8(a) depicts the "front-to-I-side" layout, while Fig. 8(b) shows the "front-to-front" layout, and Fig. 8(c) shows the "I-side-to-I-side" layout.

We consider three types of layouts for the proposed 2 × 1 MIMO antenna structure and their effects on impedance bandwidth, isolation, and axial ratio. Figure 9 shows how the layouts affect S_{11}, isolation, and axial ratio. The first case, a (front-to-I-side) layout, is illustrated in Fig. 9 (a). The reflection coefficient is deformed compared to a single monopole, especially at Band 1, while the isolation is around 16 dB over the whole first band; the axial ratio is degraded where the minimum value is 3.3 dB at 6.8 GHz. Figure 9 (b) illustrates the (front-to-front) layout in the second scenario. Although the S_{11} and S_{22} are restored as in a single monopole at both bands, the isolation and axial ratio are severely distorted to 7 dB in Band 1 and around 11 dB in Band 2 for isolation, and the minimum value for AR is 5 dB within Band 2.

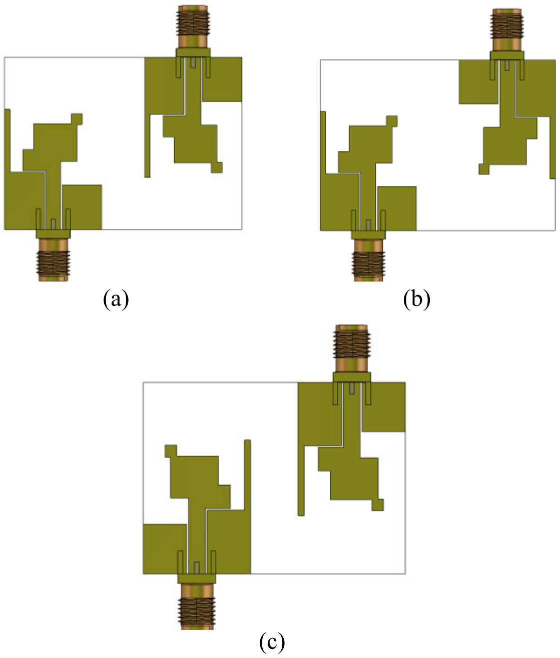

FIGURE 8. Layouts for the 2 × 1 MIMO SMMGD antenna structure (a) front-to-I-side orientation (b) front-to-front orientation (c) I-side-to-I-side.

Finally, Fig. 9(c) depicts the third scenario (I-side-to-I-side) configuration. In this configuration, both bands of S_{11} and S_{22} <-10 dB are restored; even impedance bandwidth for band 2 is improved compared with a single patch and extends from 5.1 GHz to 8 GHz, while the axial ratio of less than 3 dB covers the range from 6 GHz to 8 GHz.

A. COMMON PARTIAL GROUND AND DECOUPLING STRUCTURE

With I-side-to-I-side, the antenna achieved good impedance bandwidth and axial ratio. This design introduces MIMO elements with an orthogonal sense of polarization providing.

RHCP along +Z and LHCP along -Z directions introduce pattern and polarization diversity. However, it is still a scarce common ground among MIMO elements, which keeps their axial ratio, isolation, and frequency response like those without a common ground due to the leakage in the current among partial grounds.

Figure 10 presents the I-side-to-I-side of the opposite orientation of 2 × 1 MIMO's common ground evolution steps. As shown in Fig. 10, we may resume the Naturalization

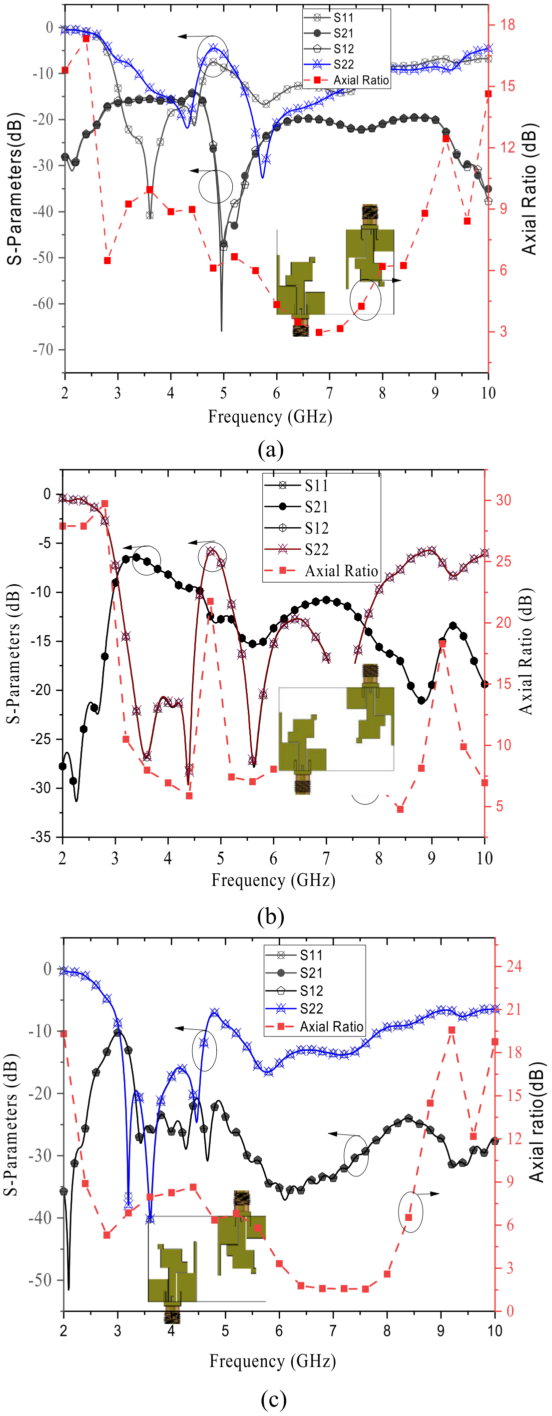

FIGURE 9. Scattering parameters and axial ratio for 2 × 1 MIMO antenna structure (a) front-to-I side (b) front-to-front layout (c) I side-to-I side layout.

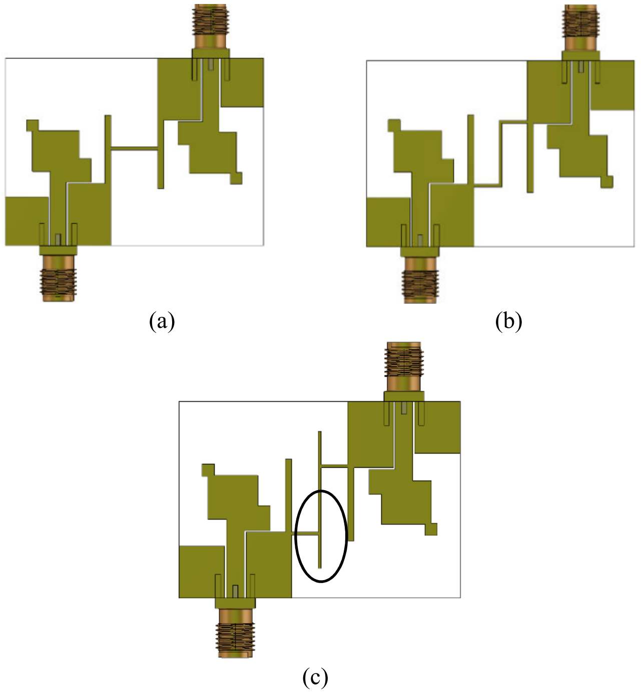

FIGURE 10. Common partial ground evolution (a) bridge shape strip (b) stair step shape strip (c) double T-shape strip sharing a common head.

Line (NL) as common ground evolution through three steps: a bridge strip, a stair-step strip, and Double T-shaped strips (DTSS) with shared heads.

Figure 11 illustrates the common ground evolution steps' S_{11}, S_{22}, isolation, and axial ratio. Figure 11 (a) shows the bridge strip type where the S_{11}, S_{22}, and isolation are shifted to a higher frequency in the sub-6 GHz of band 1, ranging from 3.7 GHz to 5 GHz, compared without common partial ground. However, this common partial ground shows good AR bandwidth below 3 dB between 6 and 8.5 GHz. Further analysis uses the stair-step strip common partial ground design in Fig. 11(b). It shows that this design restores the S_{11} and S_{22} to those without common partial ground and also enhances the isolation to reach a minimum of 18 dB in band 1 and 24 dB in band 2. However, as shown in Fig. 11(b), the axial ratio bandwidth below 3 dB narrows to a confined range of 5.8 GHz to 7.5 GHz.

Finally, a DTSS with shared common heads connected to the partial ground is proposed as an NL. The idea is to create a flow of current 180 degrees out of phase between the two connected antenna grounds. Figure 12 illustrates the equivalent circuit of a DTSS decoupling structure. The equivalent circuit comprises three parts: the inductance (L), the resistance (R), and the capacitance (C). The DTSS structure acts as a series band-stop filter and controls how the current flows between the SMMDGs. The equivalent circuit comprises three parts: the inductance ($L = 1.6$ nH), the resistance ($R = 70$ ohms), and the capacitance ($C = 0.952$ pF) are calculated using ADS software.

Figure 13 shows the surface current at 3.5 GHz at phase angles 0° and 180° of the DTSS. To visualize the current distribution at band 1, as shown in Fig. 13(a), the surface currents at 0° in the T-shape necks (regions 1 and 2) of the DTSS decoupling are in opposite directions and out of phase.

The same thing can be seen with I-strips for both antennas, where the surface current points in opposite directions in the common head of a DTSS, as seen in regions 3 and 4 in Fig. 13(a). The same behavior of the surface current

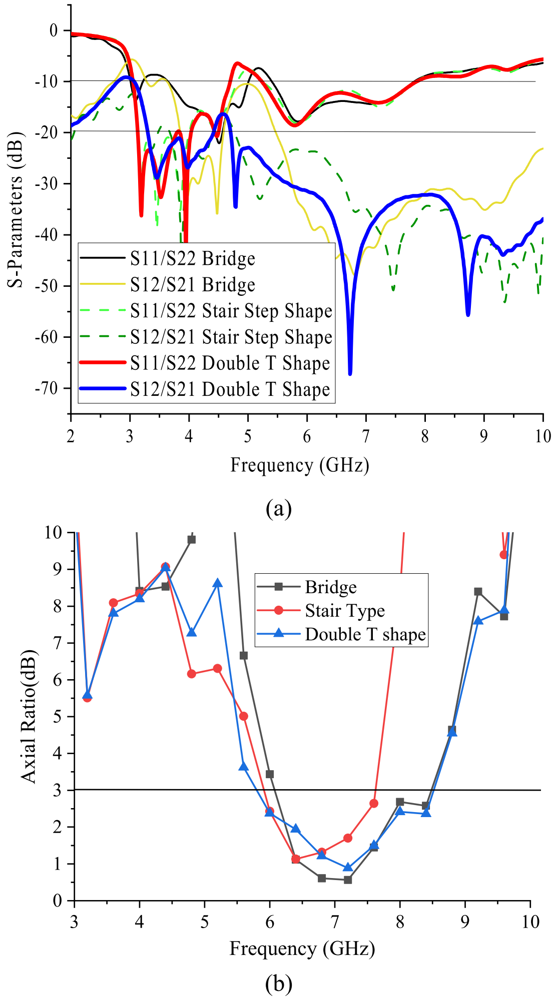

(a)

(b)

FIGURE 11. Common partial ground evaluation effect (a) S-parameters (b) axial ratio.

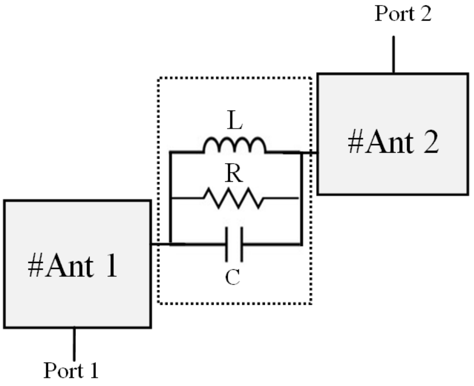

FIGURE 12. A stop-band filter equivalent circuit model for the (L = 1.6 n, R = 70 ohm, C = 0.952 pF) double T-shape strips (DTSS).

distribution at 180° can be seen, but in the opposite direction, as shown in Fig. 13(b), demonstrating the rejection coupling between MIMO elements.

Back to Fig. 11(a), and as discussed for the DTSS structure, which stands for NL, behaves as a band stop filter, isolation is enhanced to more than 21 dB in the sub-6 GHz band 1 and less than 29 dB in band 2, while in Fig. 11(b), the axial ratio bandwidth below 3 dB is extended to 5.6 GHz–8.5 GHz, where the frequency response for both bands is restored as in the single element.

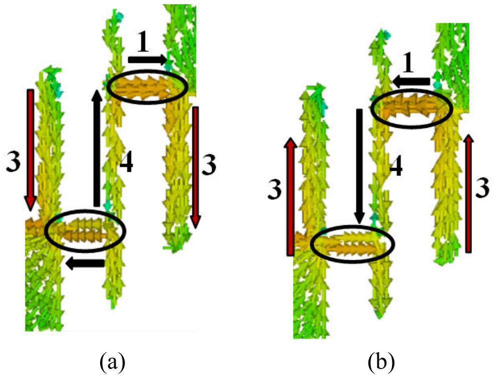

(a) (b)

FIGURE 13. Surface current on the double T strips decoupling structure at 3.5 GHz (a) wt = 0° (b) wt = 180°.

Figure 14 shows the final 2 × 1 MIMO antenna geometry and prototype with an opposite configuration, I-side to I-side layout, and a DTSS of a common head as a common partial ground. As shown in Fig. 14(a), the antenna unit on the left side is designated Antenna 1, while the other is designated Antenna 2. The overall dimension is 31.5 × 45 × 1.6 mm^3, while Fig. 14 (b) depicts the fabricated prototype.

Figure 15 (a) shows the simulated and measured frequency response of the scattering parameters, and Fig. 15 (b) shows the simulated and measured axial ratios. As shown in Fig. 15 (a), the simulated and measured results of band 1 for S_{11} and $S_{22} < -10$ dB are 3.1 GHz–4.7 GHz and 3.45 GHz–4.8 GHz, respectively. The simulated bandwidth for S_{11} and $S_{22} < -10$ dB of band 2 covers 5.24 GHz–7.9 GHz, while the measurement is 5.95 GHz–9 GHz. The minimum simulated isolation of band 1 is over 17 dB, while the minimum measured isolation is 21 dB. The minimum measured isolation for band 1 is over 21 dB, while the minimum for band 2 is over 26 dB. Figure 15(b) shows the simulated and measured axial ratios, where the overlapped results of ARBW are between 5.95 GHz and 8.1 GHz of below 3 dB. As shown in Fig. 15 (a), the overlapped simulation results with measurements are highlighted in green for bands 1 and 2. Band 1 provides a 3.45–4.7 GHz bandwidth with a minimum isolation of 21 dB. Band 2 is confined between 5.65 GHz and 7.8 GHz with a minimum isolation of 26 dB.

A good agreement is observed between the simulation and measured values of S_{11} and S_{22}. The observed inheritable discrepancies are mostly attributed to the prototype tolerances and limited resolution of simulation results.

B. RADIATION PATTERNS

Figure 16 shows the polar radiation patterns at 3.5 GHz and 6 GHz. Both simulated and measured patterns in the (x-z) plane corresponding to normalized gain (θ); $\emptyset = 0°$

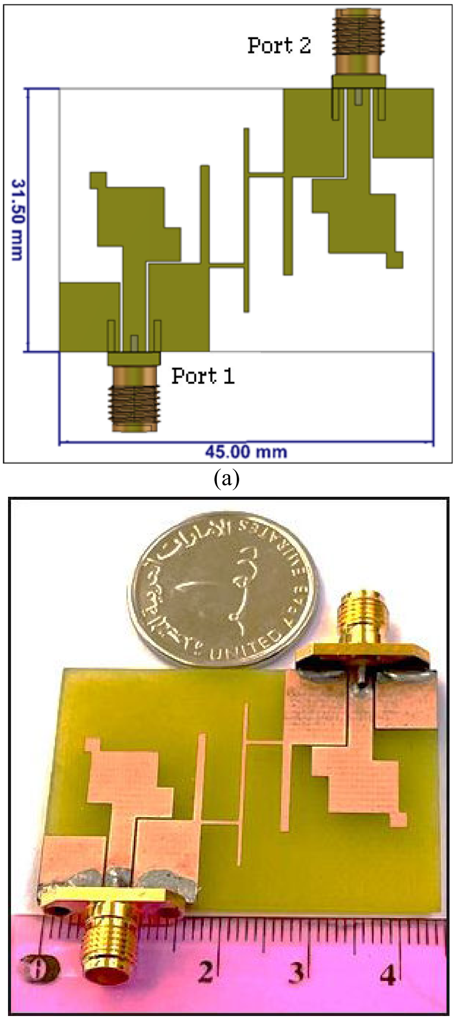

(a)

(b)

FIGURE 14. **MIMO antenna with double T strips decoupling structure (a) Geometry (b) Fabricated prototype.**

and in the (y-z) plane corresponding to normalized gain (θ); $\emptyset = 90°$ are presented.

As shown in Fig. 16(a), the simulated and measured radiation pattern of the (x-z) plane of port 1 is shown, while Fig. 16(b) shows the (x-z) plane of port 2 at 3.5 GHz. The (x-z) plane takes the directive in the 270° direction in port 1, while in port 2, the directive is in the 90° direction.

Figures 16(c) and (d) show the simulated and measured (y-z) plane radiation patterns of ports 1 and 2, respectively, at 3.5 GHz. At port 1, the directive points to 180°, while it points to 0° in port 2. Figures 16(a-d) show the co and cross patterns at band 1.

Figure 16 (e and f) depict RHCP waves' (x-z) plane patterns at 6 GHz for ports 1 and 2, respectively. The simulated and measured (x-z) plane patterns at 6 GHz are shown in Fig. 16(e) when port 1 is excited and port 2 is terminated with a 50Ω. Its pattern shows directives in 270°. Figure 16(f) shows the radiation pattern of the (x-z) plane when port 2 is excited and port 1 is connected to a 50Ω load at a frequency

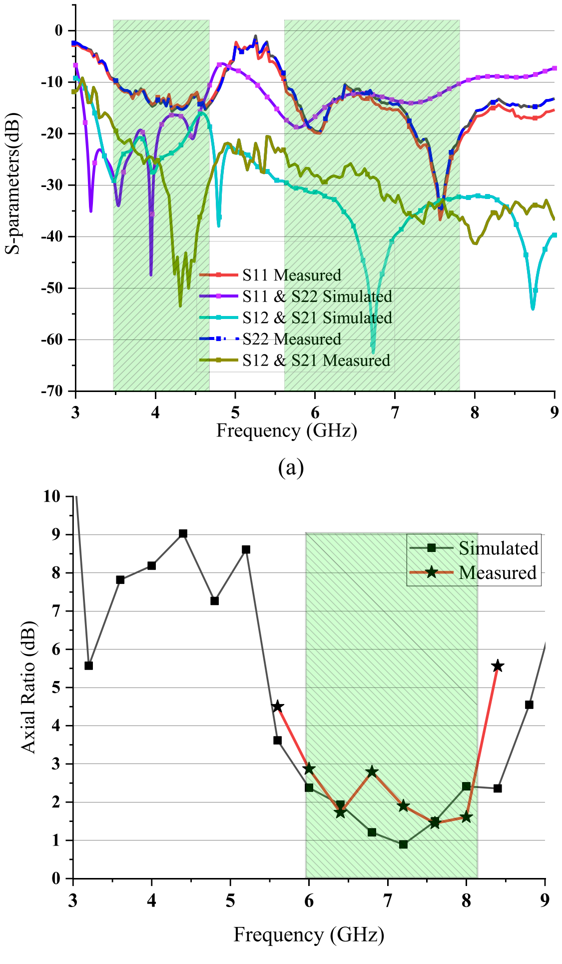

FIGURE 15. **Simulated and measured S-parameters and axial ratio.**

of 6 GHz. Its pattern shows directives in 90°. Figure 16(g) shows the (y-z) plane of the radiation pattern when port 1 is excited and port 2 is connected to a 50Ω load at a frequency of 6 GHz. The pattern of port 1 at 6 GHz skews its directive into 330° and 210°. In Fig. 16(h), which shows the (y-z) plane pattern of port 2, the radiation pattern skews its directive points to 30° and 150°, which is the mirror pattern as in Fig. 16(g).

The simulated and measured patterns in the (x-y) plane corresponding to the gain ($\emptyset$) of $\theta = 90°$ are also presented in Figs. 16(i) and 16(j) for ports 1 and 2, respectively. Figure 16(i) shows the simulated and measured pattern of RHCP waves radiating in the x-y plane when port 1 is excited. This shows more directive in 210°. Figure 16(j) shows the radiation pattern in the (x-y) plane with port 2 excited, which shows its directive in 30°. However, in Fig. 16 (e-j) for band 2, the patterns described above are RHCP in the +Z direction, but the mirror radiation patterns are also depicted as LHCP in the -Z direction. The simulated and measured radiation patterns of port 2 are RHCP waves in the +Z direction and emit as a mirror in the -Z direction as RHCP but in the

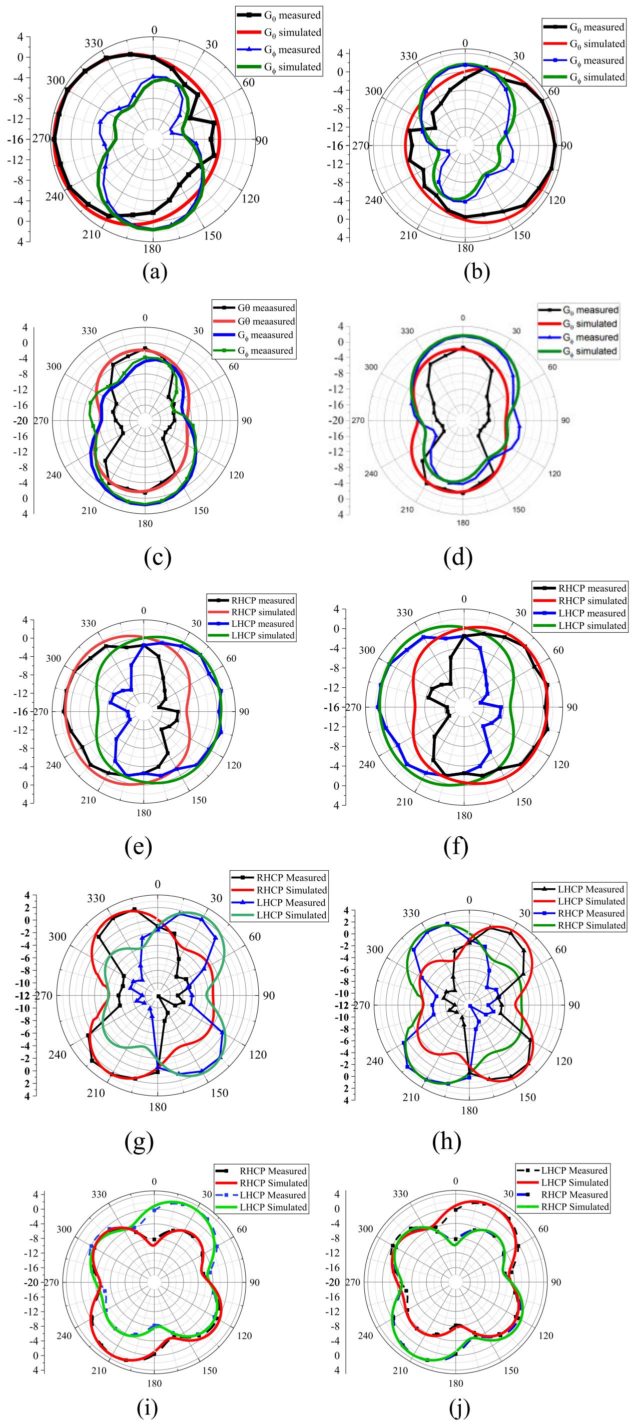

FIGURE 16. Simulated and measured radiation pattern (a) (x-z)plane of port 1 at frequency 3.5 GHz (b) (x-z) plane port 2 at frequency 3.5 GHz (c) (y-z) plane with port 1 at 3.5 GHz (d) (y-z) plane with port 2 at 3.5 GHz (e) (x-z) plane with port 1 excited at 6 GHz (f) (x-z) plane port 1 at 6 GHz (g) (y-z) plane port 1 at 6 GHz (h) (y-z) plane port 2 at 6 GHz (i) (x-y) plane at 6 GHz port 1 (j) (x-y) plane at 6 GHz port 2.

opposite direction to the radiation pattern of port 1. These complementary properties of the pattern make it possible for the proposed MIMO antenna to create pattern and polarization diversity.

Figure 17 shows the simulated 3D radiation pattern for both ports at 3.5 and 6 GHz. As illustrated in Fig.17 (a) at 3.5 GHz, the 3D pattern shows the complementary patterns of port 1 compared to Fig. 17(b) of port 2 that support pattern diversity. The same observation can be seen in Fig.17 (c) for port 1 as compared with Fig. 17(d) the complementary radiation pattern supports diversity.

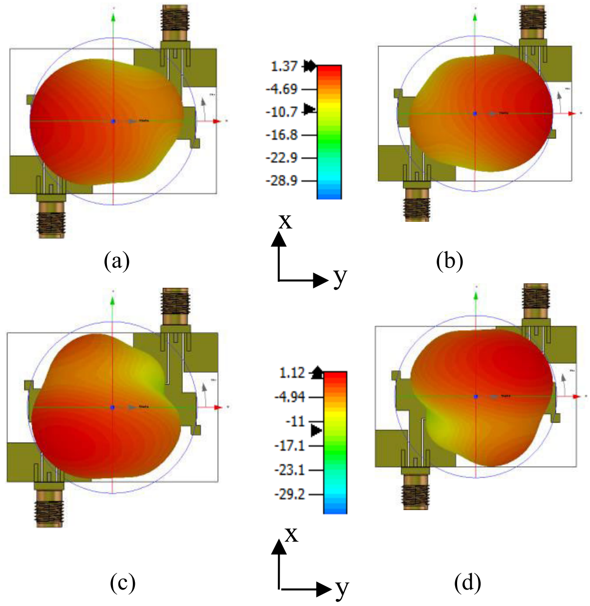

FIGURE 17. 3D radiation pattern (a) port 1 at 3.5 GHz (b) port 2 at 3.5 GHz (c) port 1 at 6 GHz (d) port 2 at 6 GHz.

Figure 18 shows the simulated and measured gain versus frequency plotted on the left side, while the right side of the plot is the simulated radiation efficiency. The Band 1 gain is between 1.8 and 3.5 dBi, while the gain in Band 2 varies from 3.5 to 4.5 dBi. Band 1 has a minimum radiation efficiency of 87%, while band 2 has a minimum radiation efficiency of 85%.

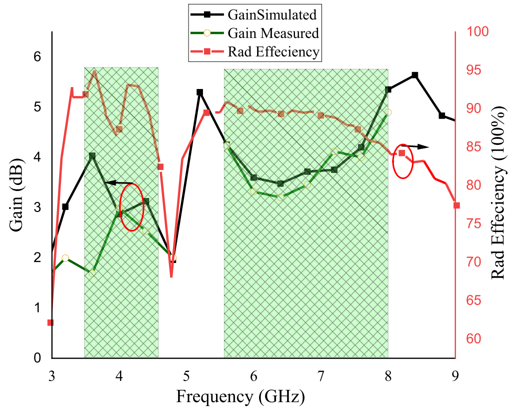

FIGURE 18. Simulated and measured gain vs. frequency (left side) and simulated radiation efficiency (left side).

TABLE 2. Comparison to the previous work.

Ref. No.	Dimensions (Corresponds to lower frequency mm3/Substrate Specifications	Isolation (dB)	BW GHz	ECC	Gain (dBi)	Polarization/Type	3-dB ARBW	No. of ports/Common ground
[31]	0.74λ0× 0.96λ0 × 0.021λ0/Textile , ε_r =1.34 , tanδ =0.02	≥ 18	3.6-13	<0.02	-1-5.7	C.P/LHCP-RHCP	5.2 -7.1	**2/Yes**
[32]	0.74λ0 × 0.42 λ0 × 0.11λ0/ FR4, ε_r =4.3 , tanδ =not given	> 25	1.8-2.6	< 0.01	3-4	C.P/LHCP-RHCP	2.2-2.6	**2/Yes**
[33]	1.5λ0×0.5λ0×0.01 λ0/ Rogers RO4003, εr =3.38 , tanδ =0.0027	> 20	2.9-7.1	<0.003	~ 3.5	C.P/LHCP-RHCP	3.1-6.35	**2/No**
[6]	0.69λ0 × 0.26λ0 ×0.015λ0/ Rogers RO4003C, εr =3.83 , tanδ =0.0027	> 22	5.2-6.3	<0.004	~ 3.5	C.P/LHCP-RHCP	5.2-6.3	**2/No**
[34]	0.46λ0×0.37λ0×0.009λ0 /FR-4 , ε_r =4.4, tanδ = 0.019	>15	3.3-4.2	<0.1	1 - 3	C.P/LHCP-RHCP	3.3-4.2	**2**/Yes
[35]	1.14λ0×0.91λ0×0.05λ0/Taconic TLY substrate , ε_r = 2.2, tanδ =0.0009	≥ 22	4.8–5.8	<0.01	7.5 - 8.2	C.P/ LHCP-RHCP	5.1-5.8	**2**/ Yes
[36]	0.96λ0×0.43λ0 ×0.08 (addition air thick(3mm) / FR-4 , ε_r =4.3, tanδ = 0.025	≥ 37	5.2–6.4	<0.001	5.5-6	C.P/ LHCP-RHCP	5.37 - 5.72	**2**/NO
[7]	0.39λ0 ×0.39λ0 ×0.026λ0/ FR-4 , ε_r =4.3, tanδ = not given	≥ 16	3.04-8.11	<0.004	0.28 - 2.76	C.P/ LHCP	4.42-6.11	**2**/ Yes
[37]	0.9λ0 ×0.83λ0 ×0.12λ0/ FR-4 , ε_r =4.4, tanδ = 0.02	≥ 18	3-7	<0.21	3.5-4	L.P	-	**2**/ Yes
[38]	1.82λ0 ×1.82λ0 ×0.11λ0/ FR-4 , ε_r =4.4, tanδ = 0.02	≥ 15	5.71–8.2	<0.05	3.5-3.8	C.P	7.72–8.04	**2**/ Yes
[39]	1.34λ0×0.77λ0×0.3 λ0/ FR-4 , 4.3, tanδ = 0.025	>30	4.89–6.85	<0.002	6- 6.45	LP/C.P	5.41–6.57	**2**/ Yes
[40]	0.74λ0 × 0.93λ0 × 0.14λ0 / FR-4 , 4.3, tanδ = 0.025	>25	5.25-6	<0.12	4.3-4.7	C.P/RHCP-LHCP	4.3-4.7	**2**/ Yes
[41]	0.68λ0 × 0.68λ0 × 0.018λ0 / FR-4 , 4.4, tanδ = 0.02	>19	3.4–3.8	<0.12	4-4.5	C.P/RHCP-LHCP	3.46–3.7	**4/**Yes
This Work	0.6 λ0 × 0.41 λ0 × 0.021 λ0 / FR-4 , 4.3, tanδ = 0.025	Band 1 >17 Band 2 >26	3.45-4.7 5.45-9	<0.009	2.5-3.4 3.5-4	LP/C.P LHCP +Z RHCP -Z	5.95-8.1	**2**/ Yes

IV. PERFORMANCE OF THE PROPOSED MIMO ANTENNA

To demonstrate the diversity performance of the proposed MIMO antenna, we evaluated the Envelope Correlation Coefficient (ECC), Diversity Gain (DG), and Mean Effective Gain (MEG).

Low correlations should be achieved to improve the MIMO antenna element's performance. Acceptable ECC limits are between 0 and 0.5 [24]. The ECC is evaluated by S-parameters using the following formula [25].

$$ECC = \frac{\left|S_{11}^{*}S_{21} + S_{21}^{*}S_{22}\right|^{2}}{\left(1 - (|S_{11}|^{2} - |S_{21}|^{2})\right)\left(1 - (|S_{22}|^{2} - |S_{12}|^{2})\right)} \quad (1)$$

where the complex conjugate of S_{11} and S_{21} are denoted as S_{11}^{*} and S_{21}^{*}, respectively.

The far fields may be used to compute ECC to get a more accurate result [26] as:

$$ECC = \frac{|\iint 4\pi[R_1(\theta,\Phi).R_2(\theta,\Phi)d\Omega]|^2}{\iint 4\pi|R_1(\theta,\Phi)|^2 d\Omega \iint 4\pi|R_2(\theta,\Phi)|^2 d\Omega} \tag{2}$$

$R_i\,(\theta, \emptyset)$ refers to the radiation pattern when port (i) is excited, and Ω refers to the solid angle.

With the use of DG, it is also possible to test how well a MIMO antenna performs. Though a DG of 10 dB is ideal, values of 6 dB or above are still desirable [27]. The following approximate expression is used to calculate the diversity gain [28]:

$$DG = 10\sqrt{1-(ECC)^2} \tag{3}$$

The scattering parameters and far-field versus frequency approaches for calculating ECC are shown in Fig. 19; along with DG, it shows excellent performance from 3.4 GHz to 4.5 GHz (band 1) and 5.6 GHz to 7.8 GHz (band 2) with an ECC much below 0.002 obtained using S-parameters and an ECC of 0.009 obtained using the far fields. This outcome is much lower than the acceptable values for MIMO systems. In addition, the antenna system achieves outstanding diversity gain (DG > 9.98 dB) throughout the two bands.

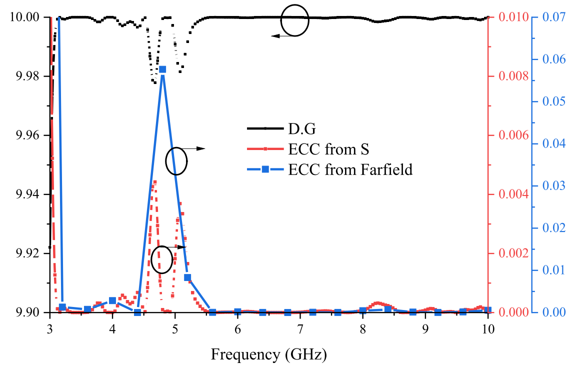

FIGURE 19. Simulated envelope correlation coefficient (ECC) using S-parameters and radiation pattern, including DG against frequency.

The MEG is another important MIMO parameter. MEG is the ratio between the diversity antenna's mean power and the isotropic antenna's mean received power. The best range for each MEG value is between −12 dB and −3 dB. MEG is calculated using the formula given in [29]:

$$MEG_{(i)} = 0.5\left(1-\sum_{j=1}^{n}|S_{ij}|^2\right) \tag{4}$$

In addition, the absolute difference between MEG1 and MEG2 should be below 3 dB for ideal performance [30]. Fig. 20 illustrates the computed MEG1, MEG2, and value of |MEG1-MEG2|. It is clear that EMG1 and EMG2 are near the desired value of −3 dB, and their |EMG1- EMG2| is close to 0 dB, indicating compliance with optimal MIMO metrics.

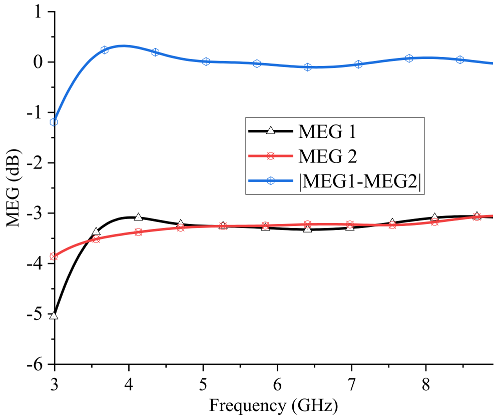

FIGURE 20. Simulated mean effective gain MEG1, MEG2, and |MEG1-MEG2| versus frequency of the proposed SMMGD MIMO antenna.

V. PROPOSED ANTENNA PERFORMANCE COMPARISON AGAINST STATE-OF-THE-ART

Table 2 compares our proposed MIMO antenna against typical designs reported during the past five years. The table shows that our design performs well in overall MIMO attributes, whether by bandwidth, ARBW, gain, ECC, size, or isolation. Moreover, compared to other designs, its simple design has a small footprint, wide ARBW, good isolation, and small ECC. All these attributes make the proposed antenna a good candidate for MIMO applications.

VI. CONCLUSION

This paper presents and experimentally validates a two-port, compact, easy-to-fabricate, dual-band MIMO antenna. The single element is a CPW-fed Square Shape Modified Monopole with Defecated Partial Ground (SMMDG). Two bands are evaluated: band 1 is dedicated to the sub-6 band with linear polarization and spatial diversity, covering (3.45 – 4.7) GHz with S_{11} and $S_{22} < -10$ dB, where the minimum isolation through this band is 17 dB. The second band covers 5.6 GHz –7.8 GHz for which S_{11} and $S_{22} < -10$ dB, including the Wi-Fi 6E (n96) (5.925 - 7.125) GHz with left-hand circular polarization (LHCP) in a +Z of less than 3 dB axial ratio bandwidth of 5.95 GHz – 7.8 GHz. The Wi-Fi 6E band supports both spatial and pattern diversity. The minimum isolation through band 2 is 26 dB. The two elements emit bidirectional patterns, with an LHCP in the +Z direction and an RHCP in the -Z direction. Other MIMO metrics, such as ECC, MEG, and DG, are examined and show their conformity with features of MIMO technology. Because it has excellent MIMO diversity and antenna performance for wireless communications, the proposed antenna can be used in a wide range of wireless applications.

REFERENCES

[1] M. K. Shereen, M. I. Khattak, and J. Nebhen, "A review of achieving frequency reconfiguration through switching in microstrip patch antennas for future 5G applications," *Alexandria Eng. J.*, vol. 61, no. 1, pp. 29–40, Jan. 2022, doi: 10.1016/j.aej.2021.04.105.

[2] J. Khan, D. A. Sehrai, M. A. Khan, H. A. Khan, S. Ahmad, A. Ali, A. Arif, A. A. Memon, and S. Kha, ''Design and performance comparison of rotated Y-shaped antenna using different metamaterial surfaces for 5G mobile devices,'' *Comput., Mater. Continua*, vol. 60, no. 2, pp. 409–420, 2019, doi: 10.32604/cmc.2019.06883.

[3] R. Sharma, R. Khanna, and Geetanjali, ''Compact sub-6 GHz and mmWave 5G wideband 2 × 1 MIMO antenna with high isolation using parasitically placed double negative (DNG) isolator,'' *Wireless Pers. Commun.*, vol. 122, no. 3, pp. 2839–2857, Feb. 2022, doi: 10.1007/s11277-021-09032-8.

[4] A. Patel, A. Desai, I. Elfergani, A. Vala, H. Mewada, K. Mahant, S. Patel, C. Zebiri, J. Rodriguez, and E. Ali, ''UWB CPW fed 4-port connected ground MIMO antenna for sub-millimeter-wave 5G applications,'' *Alexandria Eng. J.*, vol. 61, no. 9, pp. 6645–6658, Sep. 2022, doi: 10.1016/j.aej.2021.12.015.

[5] G. Naik, J.-M. Park, J. Ashdown, and W. Lehr, ''Next generation Wi-Fi and 5G NR-U in the 6 GHz bands: Opportunities and challenges,'' *IEEE Access*, vol. 8, pp. 153027–153056, 2020, doi: 10.1109/ACCESS.2020.3016036.

[6] U. Ullah, I. B. Mabrouk, and S. Koziel, ''Enhanced-performance circularly polarized MIMO antenna with polarization/pattern diversity,'' *IEEE Access*, vol. 8, pp. 11887–11895, 2020, doi: 10.1109/ACCESS.2020.2966052.

[7] R. N. Tiwari, P. Singh, B. K. Kanaujia, and P. Kumar, ''Compact circularly polarized MIMO printed antenna with novel ground structure for wideband applications,'' *Int. J. RF Microw. Comput.-Aided Eng.*, vol. 31, no. 8, pp. 1–13, Aug. 2021, doi: 10.1002/mmce.22737.

[8] A. Desai, M. Palandoken, J. Kulkarni, G. Byun, and T. K. Nguyen, ''Wideband flexible/transparent connected-ground MIMO antennas for sub-6 GHz 5G and WLAN applications,'' *IEEE Access*, vol. 9, pp. 147003–147015, 2021, doi: 10.1109/ACCESS.2021.3123366.

[9] P. Kumar, S. Urooj, and A. Malibari, ''Design and implementation of quad-element super-wideband MIMO antenna for IoT applications,'' *IEEE Access*, vol. 8, pp. 226697–226704, 2020, doi: 10.1109/ACCESS.2020.3045534.

[10] H. A. Mashagba, H. A. Rahim, I. Adam, M. H. Jamaluddin, M. N. M. Yasin, M. Jusoh, T. Sabapathy, M. Abdulmalek, A. A. Al-Hadi, A. M. Ismail, and P. J. Soh, ''A hybrid mutual coupling reduction technique in a dual-band MIMO textile antenna for WBAN and 5G applications,'' *IEEE Access*, vol. 9, pp. 150768–150780, 2021, doi: 10.1109/ACCESS.2021.3125049.

[11] W. Lin and H. Wong, ''Wideband circular polarization reconfigurable antenna,'' *IEEE Trans. Antennas Propag.*, vol. 63, no. 12, pp. 5938–5944, Dec. 2015, doi: 10.1109/TAP.2015.2489210.

[12] E. Zhang, J. Qiu, A. Michel, and P. Nepa, ''Compact dual circularly polarized patch antenna with high ports isolation for MIMO WLAN application,'' in *Proc. IEEE Int. Symp. Antennas Propag. North Amer. Radio Sci. Meeting*, Jul. 2020, pp. 603–604, doi: 10.1109/IEEECONF35879.2020.9330281.

[13] F. A. Dicandia, S. Genovesi, and A. Monorchio, ''Analysis of the performance enhancement of MIMO systems employing circular polarization,'' *IEEE Trans. Antennas Propag.*, vol. 65, no. 9, pp. 4824–4835, Sep. 2017, doi: 10.1109/TAP.2017.2723083.

[14] F. M. Alnahwi, H. L. Swadi, and A. S. Abdullah, ''Design and simulation of single and 2 × 2 MIMO circularly polarized patch antennas with a pair of chip resistors for 5G applications,'' in *Proc. Int. Symp. Multidisciplinary Stud. Innov. Technol. (ISMSIT)*, Oct. 2022, pp. 488–493, doi: 10.1109/ISMSIT56059.2022.9932653.

[15] C. A. Balanis, *Antenna Theory Analysis and Design*, 4th ed. Hoboken, NJ, USA: Wiley, 2016.

[16] N. Hussain, M.-J. Jeong, A. Abbas, and N. Kim, ''Metasurface-based single-layer wideband circularly polarized MIMO antenna for 5G millimeter-wave systems,'' *IEEE Access*, vol. 8, pp. 130293–130304, 2020, doi: 10.1109/ACCESS.2020.3009380.

[17] M. Alibakhshikenari, F. Babaeian, B. S. Virdee, S. Aïssa, L. Azpilicueta, C. H. See, A. A. Althuwayb, I. Huynen, R. A. Abd-Alhameed, F. Falcone, and E. Limiti, ''A comprehensive survey on 'various decoupling mechanisms with focus on metamaterial and metasurface principles applicable to SAR and MIMO antenna systems,''' *IEEE Access*, vol. 8, pp. 192965–193004, 2020, doi: 10.1109/ACCESS.2020.3032826.

[18] H. Yon, N. H. A. Rahman, M. A. Aris, M. H. Jamaluddin, I. K. C. Lin, H. Jumaat, F. N. M. Redzwan, and Y. Yamada, ''Development of C-shaped parasitic MIMO antennas for mutual coupling reduction,'' *Electronics*, vol. 10, no. 19, p. 2431, Oct. 2021, doi: 10.3390/electronics10192431.

[19] K. Du, Y. Wang, and Y. Hu, ''Design and analysis on decoupling techniques for MIMO wireless systems in 5G applications,'' *Appl. Sci.*, vol. 12, no. 8, p. 3816, Apr. 2022, doi: 10.3390/app12083816.

[20] C. Wei, Z.-Y. Zhang, and K.-L. Wu, ''Phase compensation for decoupling of large-scale staggered dual-polarized dipole array antennas,'' *IEEE Trans. Antennas Propag.*, vol. 68, no. 4, pp. 2822–2831, Apr. 2020, doi: 10.1109/TAP.2019.2955166.

[21] K. Wei, J.-Y. Li, L. Wang, Z.-J. Xing, and R. Xu, ''Mutual coupling reduction of microstrip antenna array by periodic defected ground structures,'' in *Proc. IEEE 5th Asia–Pacific Conf. Antennas Propag. (APCAP)*, Jul. 2016, pp. 389–390, doi: 10.1109/APCAP.2016.7843257.

[22] M. I. Ahmed, A. Sebak, E. A. Abdallah, and H. Elhennawy, ''Mutual coupling reduction using defected ground structure (DGS) for array applications,'' in *Proc. 15 Int. Symp. Antenna Technol. Appl. Electromagn.*, Jun. 2012, pp. 1–5, doi: 10.1109/ANTEM.2012.6262354.

[23] A. W. M. Saadh and R. Poonkuzhali, ''A compact CPW fed multiband antenna for WLAN/INSAT/WPAN applications,'' *AEU Int. J. Electron. Commun.*, vol. 109, pp. 128–135, Sep. 2019, doi: 10.1016/j.aeue.2019.07.007.

[24] C. Zhang, Z. Chen, X. Shi, Q. Yang, G. Dong, X. Wei, and G. Liu, ''A dual-band eight-element MIMO antenna array for future ultrathin mobile terminals,'' *Micromachines*, vol. 13, no. 8, p. 1267, Aug. 2022, doi: 10.3390/mi13081267.

[25] M. Sharma, V. Dhasarathan, S. K. Patel, and T. K. Nguyen, ''An ultra-compact four-port 4 × 4 superwideband MIMO antenna including mitigation of dual notched bands characteristics designed for wireless network applications,'' *AEU Int. J. Electron. Commun.*, vol. 123, Aug. 2020, Art. no. 153332, doi: 10.1016/j.aeue.2020.153332.

[26] X.-L. Liu, Z.-D. Wang, Y.-Z. Yin, J. Ren, and J.-J. Wu, ''A compact ultrawideband MIMO antenna using QSCA for high isolation,'' *IEEE Antennas Wireless Propag. Lett.*, vol. 13, pp. 1497–1500, 2014, doi: 10.1109/LAWP.2014.2340395.

[27] A. Ali et al., ''Mutual coupling reduction through defected ground structure in circularly polarized, dielectric resonator-based MIMO antennas for sub-6 GHz 5G applications,'' *Micromachines*, vol. 13, no. 7, p. 1082, Jul. 2022, doi: 10.3390/mi13071082.

[28] P. Palanisamy and M. Subramani, ''Design of metallic via based octa-port UWB MIMO antenna for IoT applications,'' *IETE J. Res.*, vol. 69, no. 5, pp. 2446–2456, Jul. 2023, doi: 10.1080/03772063.2021.1892540.

[29] S. Tariq, S. I. Naqvi, N. Hussain, and Y. Amin, ''A metasurface-based MIMO antenna for 5G millimeter-wave applications,'' *IEEE Access*, vol. 9, pp. 51805–51817, 2021, doi: 10.1109/ACCESS.2021.3069185.

[30] X. Tang, Z. Yao, Y. Li, W. Zong, G. Liu, and F. Shan, ''A high performance UWB MIMO antenna with defected ground structure and U-shape branches,'' *Int. J. RF Microw. Comput.-Aided Eng.*, vol. 31, no. 2, pp. 1–14, Feb. 2021, doi: 10.1002/mmce.22270.

[31] S. Kumar, D. Nandan, K. Srivastava, S. Kumar, H. Singh, M. Marey, H. Mostafa, and B. K. Kanaujia, ''Wideband circularly polarized textile MIMO antenna for wearable applications,'' *IEEE Access*, vol. 9, pp. 108601–108613, 2021, doi: 10.1109/ACCESS.2021.3101441.

[32] I. Adam, M. N. M. Yasin, N. Ramli, M. Jusoh, H. A. Rahim, T. B. A. Latef, T. F. T. M. N. Izam, and T. Sabapathy, ''Mutual coupling reduction of a wideband circularly polarized microstrip MIMO antenna,'' *IEEE Access*, vol. 7, pp. 97838–97845, 2019.

[33] U. Ullah, I. B. Mabrouk, S. Koziel, and M. Al-Hasan, ''Implementation of spatial/polarization diversity for improved-performance circularly polarized multiple-input-multiple-output ultra-wideband antenna,'' *IEEE Access*, vol. 8, pp. 64112–64119, 2020, doi: 10.1109/ACCESS.2020.2984697.

[34] A. K. Dwivedi, A. Sharma, A. K. Pandey, and V. Singh, ''Two port circularly polarized MIMO antenna design and investigation for 5G communication systems,'' *Wireless Pers. Commun.*, vol. 120, no. 3, pp. 2085–2099, Oct. 2021, doi: 10.1007/s11277-021-08461-9.

[35] J. Kulkarni, A. Desai, and C. Sim, ''Two port CPW-fed MIMO antenna with wide bandwidth and high isolation for future wireless applications,'' *Int. J. RF Microw. Comput.-Aided Eng.*, vol. 31, no. 8, pp. 1–16, Aug. 2021, doi: 10.1002/mmce.22700.

[36] I. Khan, Q. Wu, I. Ullah, S. U. Rahman, H. Ullah, and K. Zhang, ''Designed circularly polarized two-port microstrip MIMO antenna for WLAN applications,'' *Appl. Sci.*, vol. 12, no. 3, p. 1068, Jan. 2022, doi: 10.3390/app12031068.

[37] T. Sengodan and M. Murugappan, *Advance in Electrical and Computer Technologies*, vol. 672. Singapore: Springer, 2020, doi: 10.1007/978-981-15-5558-9.

[38] G. Varshney, R. Singh, V. S. Pandey, and R. S. Yaduvanshi, "Circularly polarized two-port MIMO dielectric resonator antenna," *Prog. Electromagn. Res. M*, vol. 91, pp. 19–28, 2020, doi: 10.2528/pierm20011003.

[39] I. Khan et al., "A wideband high-isolation microstrip MIMO circularly-polarized antenna based on parasitic elements," *Materials*, vol. 16, no. 1, p. 103, Dec. 2022, doi: 10.3390/ma16010103.

[40] G. Das, A. Sharma, and R. K. Gangwar, "Dielectric resonator based circularly polarized MIMO antenna with polarization diversity," *Microw. Opt. Technol. Lett.*, vol. 60, no. 3, pp. 685–693, Mar. 2018, doi: 10.1002/mop.31033.

[41] S. Saxena, B. K. Kanaujia, S. Dwari, S. Kumar, H. C. Choi, and K. W. Kim, "Planar four-port dual circularly-polarized MIMO antenna for sub-6 GHz band," *IEEE Access*, vol. 8, pp. 90779–90791, 2020, doi: 10.1109/ACCESS.2020.2993897.

WATHEQ A. NEAMAH received the B.S. degree from the College of Engineering, Al-Mutansiriyah University, Iraq, in 2004, and the M.S. degree from the University of Technical Malaysia, Melaka, Malaysia, in 2012. He is currently pursuing the Ph.D. degree in electrical engineering and electronics with the College of Engineering, University of Basrah, Iraq. He is a Lecturer with the College of Engineering, University of Thi-Qar, Iraq. His research interests include multiple-input multiple-output (MIMO) and millimeter-wave antennas; wideband antennas; circularly polarized antennas, filters: BioEM effects of antennas; and radio frequency identification.

HAIDER M. AL SABBAGH (Senior Member, IEEE) received the M.Sc. degree in communications and electronics engineering from the University of Basrah, in 1996, and the Ph.D. degree from the School of Electronic Information and Electrical Engineering (SEIEE), Shanghai Jiaotong University, in 2008. He was an Academic Visitor with Loughborough University, U.K., from September to October 2012. He is currently a Professor with the University of Basrah. His research interest includes wireless and mobile communications. He is a member of the editorial board and a referee for several prestigious international journals and conferences. For two years, he was a Scholar of the Council of Assisting Refugee Academics (CARA) Organization, London, U.K. He was the Publicity Chairperson of the first international conference on electrical engineering and applications (MIC-Electrical 2014), Athena, Greece.

HUSSAIN AL-RIZZO received the Ph.D. degree from the Electrical and Computer Engineering Department, University of New Brunswick, Canada. In 2000, he joined the Systems Engineering Department, University of Arkansas at Little Rock, where he is currently a Professor of telecommunication systems engineering. He has published more than 300 papers in peer-reviewed journals and conferences proceedings, two books, eight book chapters, and four patents. His research interests include V2V, V2X, and V2I wireless systems; smart antennas; massive MIMO; flexible RF components and antennas; implantable medical devices; electromagnetic wave scattering by complex objects; design, modeling, and testing of high-power microwave applicators; precipitation effects on GPS; terrestrial and satellite frequency re-use communication systems; field operation of NAVSTAR GPS receivers; data processing and accuracy assessment; and effects of the ionosphere, troposphere, and multipath on code and carrier-beat phase GPS observations.

• • •